Thermodecomposition synthesis of WO_3/H_2WO_4 heterostructures with enhanced visible light photocatalytic properties

Jing Cao*, Bangde Luo, Haili Lin, Benyan Xu, Shifu Chen*

College of Chemistry and Materials Science, Huaibei Normal University, 100 Dongshan Road, Anhui, Huaibei 235000, China

ARTICLE INFO

ABSTRACT

Novel WO_3/H_2WO_4 heterostructures with different contents of WO_3 were synthesized through a simple thermodecomposition method. Thermogravimetry and differential thermal analysis (TG–DTA), X-ray powder diffraction (XRD), Fourier transform infrared spectrometry (FT-IR), UV–vis diffuse reflectance spectroscopy (DRS) and N_2 adsorption and desorption isotherms were employed to study the structures, morphologies, optical properties and specific surface area of the as-prepared samples. Degradation of rhodamine B (RhB) was carried out to evaluate the photocatalytic activity of samples under visible light irradiation ($\lambda > 420$ nm). WO_3/H_2WO_4 heterostructure with 51.04 wt% WO_3 presented the highest photocatalytic activity with apparent k_{app} of 0.0330 min^{-1}. The increased photocatalytic activity of WO_3/H_2WO_4 could be attributed to the formation of the heterojunction between WO_3 and H_2WO_4, which suppresses the recombination of photoinduced electron–hole pairs. Moreover, the tests of radical scavengers confirmed that $\bullet O_2^-$ and h^+ were the main reactive species for the degradation of RhB.

© 2011 Elsevier B.V. All rights reserved.

1. Introduction

Energy shortage and environmental pollution are of the two issues people mostly concerned about in current days, semiconductor photocatalysis, an ideal "green" technology [1], is highly expected to resolve these two problems. Compared to the traditional TiO_2 photocatalyst, tungsten oxide (WO_3) is a more ideal candidate, because of its small band gap energy (2.4–2.8 eV), easy preparation, nontoxicity and stability in photocatalytic oxidation (PCO) process [2–8]. However, pure WO_3 is not an efficient photocatalyst due to the fast recombination of electron–hole pairs [2–5]. Now, two methods have been developed to improve the photocatalytic performance of WO_3. The first one is to regulate the physical property of WO_3, such as morphology and particle size [9–11]. The other one is the modification of WO_3 through noble metal deposition [2–5,12–14], metal ion doping [15] and semiconductor coupling [16–29], etc.

Among them, semiconductor coupling is one of the effective strategies for separation of photoinduced electron–hole pairs and improvement of photocatalytic activities [30,31], and has been becoming a highlight in recent years. Many semiconductors (such as TiO_2 [16–18], CuO [19], Cu_2O [20], ZnO [21], WS_2 [22], AgBr [23], $BiVO_4$ [24,25], BiOCl [26], $CaFe_2O_4$ [27], $CuBi_2O_4$

[28] and $SrNb_2O_6$ [29], etc.) have been reported to couple with WO_3 to form heterostructured photocatalysts with enhanced photocatalytic performance. In addition, many ways have been adopted to synthesize WO_3-based composite photocatalysts, such as impregnation [16,19,26], peptization [18], spray pyrolysis [21], deposition–precipitation [23], spin coating [24], milling-annealing [29], co-deposition [32], sol–gel [33] methods, and so on. However, to the best of our knowledge, no study is reported through thermodecomposition (TD) method to prepare WO_3-based composite photocatalysts.

As we all know, TD method has been extensively used in synthesizing a series of metal oxides nanoparticles from hydroxide, acid anhydride or organometallic precursors, which can provide nanoparticles with a narrow particle size distribution [34,35] and high crystallinity [36] with a simple, controllable and solvent-free process. The particle size, crystallinity and morphology can be regulated by calcinations time, temperature, concentration of reagents, surfactant and decomposition ambience [34,36]. Therefore people mostly concern about the purity and crystallinity of the single metal oxides as well as the transformation process from precursor to corresponding metal oxides. However, the intermediate hybrids, partial TD products, have never been got enough attention.

In general, if the precursors are not decomposed thoroughly, they will be coexisted with the corresponding metal oxides. Perhaps it will be a simple and potential way to construct heterostructured photocatalysts with matching band potentials. However, little work has been reported for the preparation of composite

* Corresponding authors Tel.: +86 561 3806611; fax: +86 561 3803141.
  E-mail addresses: caojing@mail.ipc.ac.cn (J. Cao), chshifu@chnu.edu.cn (S. Chen).

photocatalyst through TD method, except for $In_2O_3/In(OH)_3$ [37]. Therefore, great interests drive us to explore such precursor/metal oxide system with matching band potentials that can be adopted as highly efficient visible light driven photocatalyst.

Luckily, WO_3/H_2WO_4 is a special sample that meets the above requirements. Various crystal WO_3 powders can be prepared via TD of tungsten oxide hydrates ($WO_3·nH_2O$, $n = 1/3, 1, 2$) [38]. Particularly, cubic WO_3 (c-WO_3) can be obtained by TD method at a narrow rang of temperature (200–310 °C) using H_2WO_4 as precursor [38,39]. Fig. 1 displays a possible schematic representation of the TD process of H_2WO_4 at 200–310 °C. The H_2WO_4 (sample A) has a single-octahedral WO_6 layers structure [38,40]. As can be seen, each two WO_6 layers are connected by hydrogen bonds from H_2O molecules. The c-WO_3 (sample C) has a non-distorted ReO_3-type structure consisting of a three-dimensional network of WO_6 octahedral [39,41]. Sample B displays the intermediate hybrids, WO_3/H_2WO_4, of the partial dehydration of H_2WO_4.

The advantage of this approach is easy to synthesize precursor/metal oxide composite with different molar ratios through facile control the calcinations time at given temperatures. Moreover, it can omit subsequently complicated treatment for wiping up solvent or unwanted impurity. In addition, WO_3/H_2WO_4 may have intimate touch interfaces between WO_3 and H_2WO_4.

In the present work, we synthesized WO_3/H_2WO_4 heterostructures with highly enhanced photocatalytic activity by a fast, simple and artful method through the TD of H_2WO_4 ($WO_3·H_2O$) at 300 °C. The forming process of WO_3/H_2WO_4 was investigated via thermogravimetry and differential thermal analysis (TG–DTA), X-ray diffraction (XRD), Fourier transform infrared spectrometry (FT-IR), scanning electron microscopy (SEM) and high-resolution transmission electron microscopy (HRTEM). The photocatalytic activity was carried out by degradation of rhodamine B (RhB) under visible light irradiation ($\lambda > 420$ nm). In addition, various scavengers were introduced to the photocatalytic reaction system to explore the roles of different reactive species. The possible mechanism of photocatalytic activity enhancement of WO_3/H_2WO_4 was also proposed.

2. Experimental

2.1. Preparation of catalysts

All chemicals were analytical grade and used without further purification. Deionized water was used throughout this study.

2.1.1. Preparation of H_2WO_4 precursor

The yellow H_2WO_4 nanoparticles were prepared according to our previous study [42]. 0.04 mol of sodium tungstate dihydrate ($Na_2WO_4·2H_2O$) was dissolved into 400 mL of ethanol-water solution (1:2, v/v). Then a dilute HNO_3 solution (0.1 mol/L) was added to the Na_2WO_4 solution under continuous stirring until the final pH of the solution was 2.0 at 60 °C. After being stirring for 10 h, the resulted yellow H_2WO_4 precipitate was collected, washed with deionized water for 3 times, and dried at 65 °C for 24 h.

The synthesis reaction can be expressed as:

$$Na_2WO_4 + 2HNO_3 \rightarrow H_2WO_4\downarrow + 2NaNO_3 \tag{1}$$
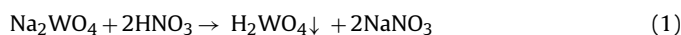
2.1.2. Synthesis of WO_3/H_2WO_4

The as-prepared H_2WO_4 sample was calcined at a constant temperature of 300 °C for 5–9 min in a Muffle furnace to obtain the WO_3/H_2WO_4 heterostructures with different contents of WO_3. The final contents of WO_3 in samples were calculated to be 1.89 wt%, 15.95 wt%, 51.04 wt%, 57.10 wt% and 93.23 wt%, respectively, by means of the reference intensity ratio (RIR) method [43–46] in the XRD patterns making use of the MDI Jade software (in Section 3.1.2). Thus, the WO_3/H_2WO_4 heterostructures were denoted as 1.89%,

15.95%, 51.04%, 57.10% and 93.23% WO_3/H_2WO_4, respectively. For comparison, pure WO_3 were also prepared via thermal treatment of H_2WO_4 at 300 °C for 30 min.

$$H_2WO_4 \xrightarrow[\text{decomposition}]{\text{partial}} WO_3/H_2WO_4 + H_2O \tag{2}$$
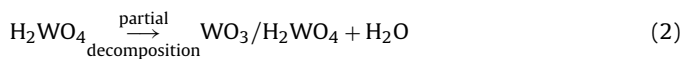
To evaluate the role of heterojunction on the photocatalytic activity of the WO_3/H_2WO_4, a mechanically mixed WO_3 and H_2WO_4 sample (denoted as $WO_3 + H_2WO_4$) was also prepared.

2.2. Characterization of catalysts

The thermogravimetry and differential thermal analysis were performed using a Shimadzu TGA-60H thermal analyzer. The atmosphere was air and the heating rate was 10 °C/min. X-ray diffraction measurements were carried out at room temperature using a BRUKER D8 ADVANCE X-ray powder diffractometer with Cu Kα radiation ($\lambda = 1.5406$ Å) and a scanning speed of 10°/min. The accelerating voltage and emission current were 40 kV and 40 mA, respectively.

The morphologies and internal structure of composites were investigated using field emission scanning electron microscopy (FEI, Sirion200, USA, scanning voltages 5.00 kV) and high-resolution transmission electron microscopy (JEOL, JEOL-2011, Japan, accelerating voltage 200 kV), respectively. UV–vis diffuse reflectance spectroscopy (DRS) measurements were carried out using a Pgeneral TU-1901 UV–vis spectrophotometer (China) equipped with an integrating sphere attachment. The analysis range was from 250 to 650 nm, and $BaSO_4$ was used as a reflectance standard. The infrared absorption spectra were recorded over the frequency range from 400 to 4000 cm^{-1} using a Nicolet 6700 FT-IR spectrophotometer (USA). The spectra were measured after the spectrum scan of the blank pure KBr pellet. A NOVA 2000e (Quantachrome Instruments, USA) instrument was used to measure the Brunauer–Emmett–Teller (BET) surface areas of the samples at liquid nitrogen temperature (77 K).

2.3. Photocatalytic activity measurements

The photocatalytic degradation of RhB was used to estimate the photocatalytic activity of WO_3/H_2WO_4 in a photoreaction apparatus [23] under visible light irradiation ($\lambda > 420$ nm). A 500 W Xe lamp (Institute of Electric Light Source, Beijing) was used as the light source with a 420 nm cutoff filter (Instrument Company of Nantong, China) to provide visible light irradiation. In each experiment, 0.1 g photocatalyst was added to 50 mL of RhB solution (10 mg/L). Prior to illumination, the suspension was magnetically stirred in the dark for 30 min to reach adsorption–desorption equilibrium of RhB on catalyst surfaces. At irradiation time intervals of 10 min, 5 mL of the suspension was collected, then centrifuged (4000 rpm, 30 min) to remove the photocatalyst particles. The catalyst-free dye solution was analyzed with a 722s spectrophotometer (Shanghai Precision and Scientific Instrument Company, China). The concentration of RhB was determined from its maximum absorption at a wavelength of 554 nm with deionized water as a reference sample.

2.4. Detection of reactive species

The examination experiment process of reactive species is similar to the photodegradation experiment. Various scavengers were introduced into the RhB solution prior to addition of the catalyst. The dosages of these scavengers were referred to the previous studies [47,48].

In addition, photoluminescence (PL) technique with terephthalic acid (TA) as a probe molecule was used to investigate the
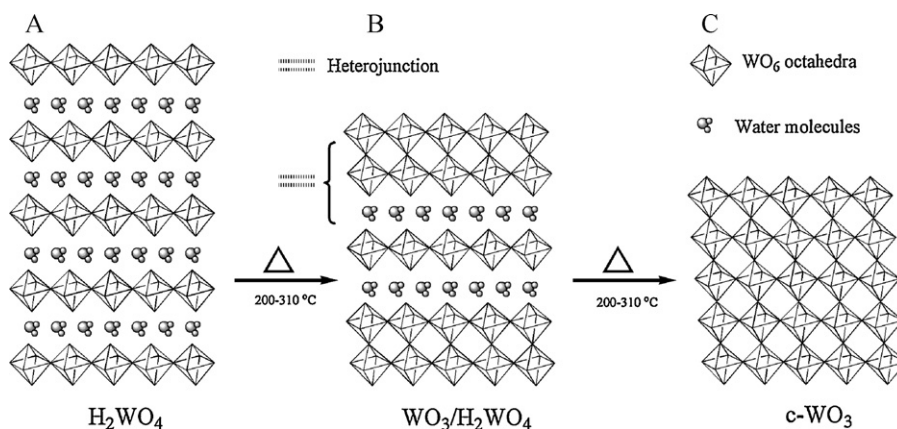
Fig. 1. A schematic representation of the thermodecomposition process of H_2WO_4 at 200–310 °C: (A) H_2WO_4 powders with single-octahedral WO_6 layers, (B) the intermediate hybrids WO_3/H_2WO_4 composite and (C) c-WO_3 with a non-distorted ReO$_3$-type structure consisting of a three-dimensional network of WO_6 octahedral.

formation of •OH radicals on the surface of WO_3/H_2WO_4 illuminated by visible light irradiation. Experimental procedures are as follows: 0.1 g of 51.04%WO_3/H_2WO_4 was dispersed in a 20 mL of the 5×10^{-4} mol/L TA aqueous solution with a concentration of 2×10^{-3} mol/L NaOH at room temperature. The same condition was applied to irradiate the above suspension as for the photocatalytic activity evaluation of catalysts (in Section 2.3). At the given time intervals, about 5 mL of the suspension was taken from the reaction suspension, centrifuged and filtered through a 0.2 μm Millipore filter to remove the particles. The filtrate was then analyzed using JASCO FP-6500 fluorescence spectrophotometer to measure the PL intensity at 425 nm induced with 315 nm excitation.

3. Results and discussion

3.1. Sample characterization

3.1.1. Thermodecomposition process

Fig. 2 shows the TG–DTA curves of H_2WO_4 precursor to understand the formation process of WO_3/H_2WO_4 heterostructures. The curves can be divided into four regions: (I) 30–180 °C, (II) 181–325 °C, (III) 326–510 °C and (IV) 511–550 °C.

In region I, there were a weight loss of 2.66% and a small endothermic peak at 51 °C, due to the evaporation of adsorbed water. In region II, a notable weight loss of 6.78% and an obvious endothermic peak at 230 °C could be found, which was attributed

to loss of the coordinated water. In this region of dehydration, majority of H_2WO_4 began to transform to crystalline c-WO_3 simultaneously [38,39]. In region III, a small endothermic and subsequently an overlapping exothermic peaks at 425 and 463 °C, respectively, corresponding to a weight loss of only 0.47%, was presented, due to the transformation of c-WO_3 to monoclinic WO_3 (m-WO_3) [38] and loss of residual coordinated water at the same time. The total weight loss of coordinated water was about 7.25%, which was almost identical to the initial theoretical value (7.20%) of pure H_2WO_4. When the temperature was higher than 510 °C, there was subsequently an overlapping exothermic effect, corresponding to no weight loss in region IV, which was also attributed to the transformation of c-WO_3 to m-WO_3 [38].

Therefore, 300 °C of calcination temperature was determined to prepare WO_3/H_2WO_4 composites, which facilitated to shorten the calcination time and obtain high crystalline product.

3.1.2. Crystalline structures

Fig. 3 shows the XRD patterns of the WO_3/H_2WO_4 with different composition ratios of WO_3 and H_2WO_4. It is observed that all the peaks of the pure H_2WO_4 (Fig. 3a) coincided with the standard orthorhombic H_2WO_4 (o-H_2WO_4) phase (JCPDS NO. 18-1418). The sample prepared via heat treatment of H_2WO_4 at 300 °C for 30 min (Fig. 3g) showed a pure c-WO_3 phase (JCPDS NO. 41-0905). In addition, the WO_3/H_2WO_4 (Fig. 3b–f) exhibited a coexistence of both c-WO_3 and o-H_2WO_4 phases. The results are consistent

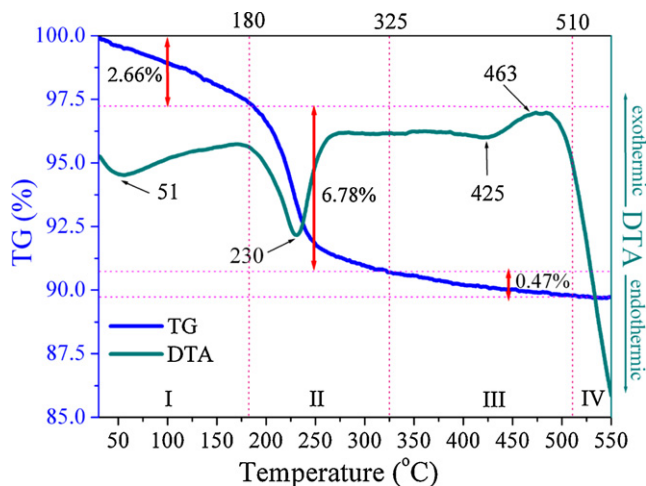**Fig. 2.** TG–DTA curves of the H_2WO_4.

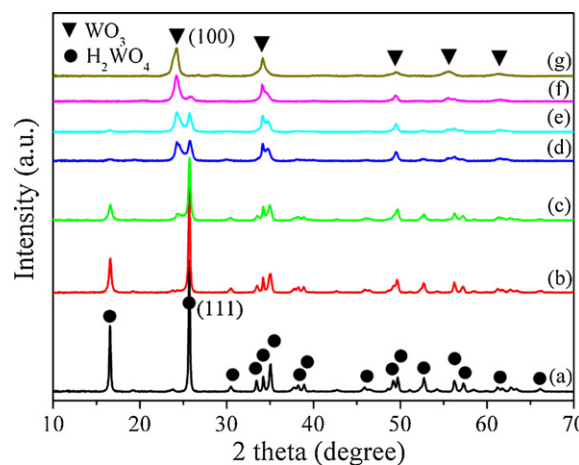**Fig. 3.** XRD patterns of H_2WO_4, WO_3 and WO_3/H_2WO_4 heterostructures: (a) H_2WO_4, (b) 1.89%WO_3/H_2WO_4, (c) 15.95%WO_3/H_2WO_4, (d) 51.04%WO_3/H_2WO_4, (e) 57.10%WO_3/H_2WO_4, (f) 93.23%WO_3/H_2WO_4 and (g) WO_3.

with the data of TG–DTA. From Fig. 3, it can be seen that, with the increase in reaction time, the intensities of diffraction peaks of c-WO_3 increased continuously whereas those of H_2WO_4 decreased simultaneously, which indicates that H_2WO_4 transformed into c-WO_3 gradually. When the sample was heat treated at 300 °C for 30 min, H_2WO_4 was totally transformed into c-WO_3, as shown in Fig. 3g.

As we all know, XRD patterns of amorphous substances are only composed of a few number of diffuse scattering peaks. However, all the XRD peaks of WO_3/H_2WO_4 were strong, sharp and consistent with the standard JCPDS card. This result suggests that the WO_3 in the as-prepared WO_3/H_2WO_4 heterostructures possess high crystallinity while an amorphous WO_3 in the WO_3/H_2WO_4 heterostructures can be neglected, even though the WO_3/H_2WO_4 heterostructures were prepared by calcining at 300 °C for a short time (5–9 min). In addition, none of other phases was observed except for o-H_2WO_4 and c-WO_3.

Composition quantitative analysis of the samples was performed on multi-phase patterns by the RIR method [43–46]. The RIR values of different samples were summarized and recognized by The International Centre for Diffraction Data (ICDD). This can also be defined as the integrated intensity ratio of the strongest peak of sample A to that of corundum (α-Al_2O_3), when sample A and α-Al_2O_3 are evenly mixed according to the mass fraction ratio of 1:1. Therefore, the RIR of sample A (RIR_A) can be calculated with the following equation:

$$RIR_A = \frac{K_A}{K_c} = \frac{I_A}{I_c} \tag{3}$$

where K_A and K_c are the reference intensities of sample A and α-Al_2O_3, respectively; I_A and I_c are integrated intensities of the strongest peak of sample A and α-Al_2O_3, respectively.

Based on the RIR values, the percentage composition can be analyzed by the application of the "adiabatic principle" if all components are crystalline and identified [43]. Particularly, when the sample is only consisted of two phases, the RIR values can be read from the PDF database and the weight ratio of each composition can be calculated using the following formula:

$$W_a = \frac{I_a}{I_a + (I_b/(RIR_b/RIR_a))} \tag{4}$$

$$W_b = \frac{I_b}{I_b + (I_a/(RIR_a/RIR_b))} = 1 - W_a \tag{5}$$

where W_a and W_b are the weight ratios of phase a and b, respectively; I_a and I_b are integrated intensities of the strongest peak of phase a and b, respectively. For H_2WO_4 and WO_3, I values determined from H_2WO_4 (1 1 1) plane and WO_3 (1 0 0) plane, respectively.

After identifying the phases in the scan pattern using MDI Jade software, the RIR values of H_2WO_4 (RIR = 27.62, JCPDS NO. 18-1418) and WO_3 (RIR = 31.10, JCPDS NO. 41-0905) could be read from the matching PDF card database. The weight ratios of WO_3/H_2WO_4 heterostructures are shown in Table 1. It is clear that the result is consistent with the analysis of Fig. 3. The average crystalline sizes of the as-prepared products are calculated according to the Scherrer formula [49] and are summarized in Table 1.

Fig. 4 presents XRD patterns of the used 57.10%WO_3/H_2WO_4 after 60 min of visible light irradiation. Both the positions and the intensities of the peaks in the XRD pattern were almost the same as those of the fresh sample, suggesting that WO_3/H_2WO_4 heterostructure is stable under visible light irradiation.

FT-IR spectra characterization was carried out to get further information on the material composition and structural characteristics. Typical FT-IR spectra of H_2WO_4, WO_3/H_2WO_4 and c-WO_3 are shown in Fig. 5. As can be seen, the strong absorption in the 500–900 cm^{-1} region was associated to the ν(O–W–O) stretching
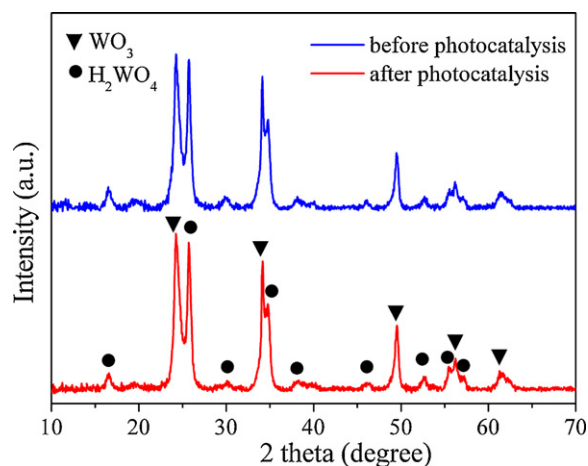

Fig. 4. XRD patterns of 57.10%WO_3/H_2WO_4 before and after visible light irradiation.

mode [50]. In the ν(O–W–O) stretching mode range, H_2WO_4 and c-WO_3 are characterized by broad bands centered around 660 and 740 cm^{-1}, respectively [38]. The positions of the infrared narrow peaks at 950 cm^{-1}, as a result of the valence vibrations of the W=O groups [51], can be used as fingerprints for H_2WO_4. The bands in the 3200–3550 cm^{-1} region are assigned to the ν(O–H) stretching vibrations (asymmetric and symmetric) of coordinated water and the band at 1625 cm^{-1} is assigned to the δ(O–H) bending vibrations of the coordinated water [50].

The FT-IR spectra of H_2WO_4 and c-WO_3 were in accordance with the previous reports [38]. Moreover, the FT-IR spectra of 15.95%WO_3/H_2WO_4 and 93.23%WO_3/H_2WO_4 were also obtained, as shown in Fig. 5, respectively. Obviously, from H_2WO_4 to c-WO_3 the ν(O–W–O) shifted to the higher frequency between 660 and 740 cm^{-1}. At the same time, the ν(W=O) at 950 cm^{-1}, well-defined peaks for H_2WO_4, as well as δ(O–H) at 1625 cm^{-1} and ν(O–H) in the 3200–3550 cm^{-1} decreased gradually from H_2WO_4 to c-WO_3 and finally disappeared till c-WO_3. These results reveal that H_2WO_4 dehydrated partially to form c-WO_3 in the TD process and then totally transformed into c-WO_3 at 300 °C for 30 min, indicating that the WO_3/H_2WO_4 heterostructures with different composition ratios of c-WO_3 and H_2WO_4 can be prepared using the TD method by controlling the calcinations time at 300 °C. Besides, no impurity or solvent residue absorption peak or absorption band was detected.
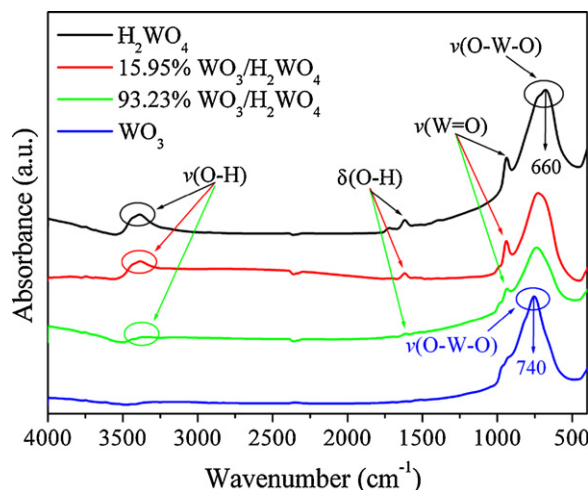

Fig. 5. FT-IR spectra of H_2WO_4, 15.95%WO_3/H_2WO_4, 93.23%WO_3/H_2WO_4 and WO_3.

Table 1
Quantitative analysis, textural properties, band gaps and photocatalytic activities of WO_3/H_2WO_4 heterostructures.

Samples	Weight ratio (wt%)		Crystalline size (nm)		BET area (m^2/g)	E_g[a] (eV)	k_{app}[b] (min^{-1})
	H_2WO_4	WO_3	H_2WO_4	WO_3			
H_2WO_4	100	0	48.5	–	23.22	2.45	0.0007
1.89%WO_3/H_2WO_4	98.11	1.89	37.8	23.5	18.77	2.46	0.0036
15.59%WO_3/H_2WO_4	84.05	15.95	27.8	13.3	17.08	2.48	0.0124
51.04%WO_3/H_2WO_4	48.96	51.04	17.5	11.8	16.12	2.50	0.0330
57.10%WO_3/H_2WO_4	42.90	57.10	16.0	11.5	17.28	2.53	0.0285
93.23%WO_3/H_2WO_4	6.77	93.23	14.1	12.1	16.38	2.64	0.0026
WO_3	0	100	–	12.7	16.45	2.68	0.0001

[a] E_g is band gap energy.
[b] k_{app} is the apparent pseudo-first-order rate constant.

3.1.3. Morphology and surface area

The morphologies of as-prepared H_2WO_4, WO_3/H_2WO_4 and WO_3 were characterized by SEM and the results are displayed in Fig. 6. From Fig. 6a, majority of H_2WO_4 powders were composed of nano-sized "square plates" with particle size of 60–250 nm, while a fraction of H_2WO_4 had acicular shapes with length between 150 and 250 nm, as well as a few of irregularly shaped nanoparticles with particle size of 4–20 nm. After TD process, H_2WO_4 nanoplates kept their morphologies whereas the H_2WO_4 acicular particles decreased gradually compared to pure H_2WO_4 (Fig. 6a). For example, 1.89%WO_3/H_2WO_4 (Fig. 6b) only had a very small fraction of acicular particles while 57.10%WO_3/H_2WO_4 (Fig. 6c) did not show any acicular particles, as well as pure c-WO_3 (Fig. 6d). Though the morphology changes suggest the decomposition of H_2WO_4, WO_3/H_2WO_4 heterojunction generally retained the morphology of H_2WO_4. In this way, WO_3 can be in situ formed and closely contact with H_2WO_4, which facilitates the efficient transfer of photoinduced carries.

The structure of the as-prepared WO_3/H_2WO_4 heterostructure was further studied by TEM and HRTEM, as shown in Fig. 7. Fig. 7a displays the typical TEM image of 57.10%WO_3/H_2WO_4, in which some nanoparticles with sizes of several nanometers were attached on the multilayer of nano-sized "square plates" with sizes of about 150 nm, consistent with the SEM observation. The HRTEM image of 57.10%WO_3/H_2WO_4 (Fig. 7b) reveals that two sets of different lattice images were found with the d spaces of 0.37 and 0.35 nm, corresponding to the (1 0 0) plane of WO_3 and the (1 1 1) plane of H_2WO_4, respectively, which are in good accordance with the results of the XRD patterns shown in Fig. 3. The results of HRTEM suggest that WO_3/H_2WO_4 nanocrystal heterojunction formed in the composites, which facilitates the separation of the photoinduced carriers and thus improve the corresponding photocatalytic activities.

BET surface area measurements of the samples were carried out at liquid nitrogen temperature, and the corresponding values are summarized in Table 1. As can be seen, the pure H_2WO_4 displays a BET area of 23.22 m^2/g while pure WO_3 displays a BET area of 16.45 m^2/g. The WO_3/H_2WO_4 heterostructures have surface areas between 18.77 and 16.12 m^2/g. These results indicate that the BET areas of the samples are changed insignificantly.

3.1.4. Optical band gap

Fig. 8 displays the DRS of the as-prepared samples. It reveals that H_2WO_4 and WO_3 had obvious absorption edges at about 530 and
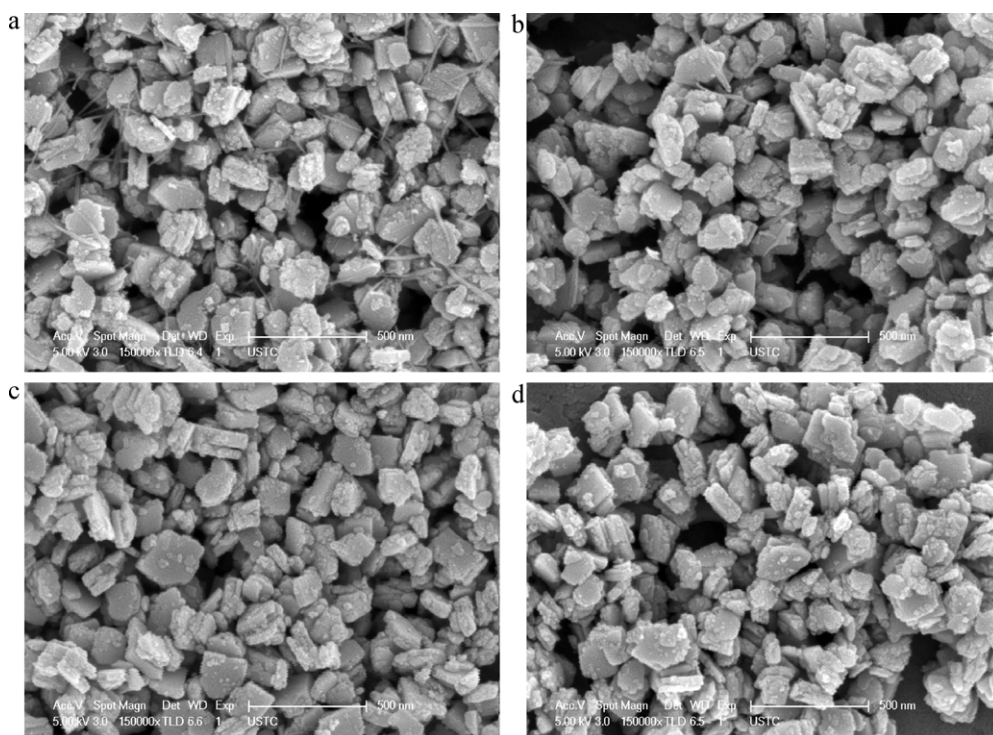

Fig. 6. SEM images of H_2WO_4, WO_3 and WO_3/H_2WO_4 heterostructures: (a) H_2WO_4, (b) 1.89%WO_3/H_2WO_4, (c) 57.10%WO_3/H_2WO_4 and (d) WO_3.

Fig. 9. Plots of $(\alpha h\nu)^2$ versus photon energy $(h\nu)$ for the band gap energies of H_2WO_4, WO_3 and WO_3/H_2WO_4 heterostructures.

The band gap energies of the as-prepared catalysts can be calculated by the following formula [52,53]:

$$\alpha h\nu = A(h\nu - E_g)^{n/2} \qquad (6)$$

where α, ν, E_g and A are absorption coefficient, light frequency, band gap energy, and a constant, respectively. Among them, n is determined by the type of optical transition of a semiconductor ($n = 1$ for direct transition and $n = 4$ for indirect transition). For H_2WO_4 and WO_3, the values of n are 1 and 1 for the indirect transition. According to Eq. (6), the band gap energy (E_g) of the resulting samples can be estimated from a plot of $(\alpha h\nu)^2$ versus energy ($h\nu$). The intercept of the tangent to the X axis would give a good approximation of the E_g of the samples (Fig. 9). Their estimated band gap energies are also summarized in Table 1. Therefore E_g of WO_3 and H_2WO_4 were found to be 2.68 and 2.45 eV, respectively. It is found that the E_g of WO_3/H_2WO_4 increased from 2.46 to 2.64 eV with the increase of WO_3 content from 1.89 to 93.23 wt%, as shown in Table 1.

The valence band (VB) edge position of WO_3/H_2WO_4 heterostructure was estimated in this study according to the concepts of electronegativity. Herein, the electronegativity of an atom is the arithmetic mean of the atomic electron affinity and the first ionization energy. The VB edge potential of a semiconductor at the point of zero charge can be calculated by flowing empirical equation [30]:

$$E_{VB} = X - E^c + 0.5E_g \qquad (7)$$

where E_{VB} is the VB edge potential, X is the electronegativity of the semiconductor, which is the geometric mean of the electronegativity of the constituent atoms, E^c is the energy of free electrons on the hydrogen scale (about 4.5 eV), E_g is the band gap energy of the semiconductor. The conduction band (CB) edge potential (E_{CB}) can be determined by $E_{CB} = E_{VB} - E_g$. The X values for WO_3 and H_2WO_4 are ca. 6.60 and 6.89 eV, and the E_{VB} of WO_3 and H_2WO_4 were calculated to be 3.44 and 3.62 eV, respectively. Thus, the E_{CB} of WO_3 and H_2WO_4 were estimated to be 0.76 and 1.17 eV, respectively.

3.2. Photocatalytic activities of WO_3/H_2WO_4 heterostructures

The photocatalytic activities of as-prepared samples were evaluated by the degradation of RhB under visible light irradiation ($\lambda > 420$ nm). Fig. 10a reveals a gradual decrease of RhB aqueous absorption at the wavelength of 554 nm under visible light irradiation.

Fig. 10b displays the photodegradation of RhB as a function of irradiation time over WO_3, H_2WO_4 and WO_3/H_2WO_4. As can be
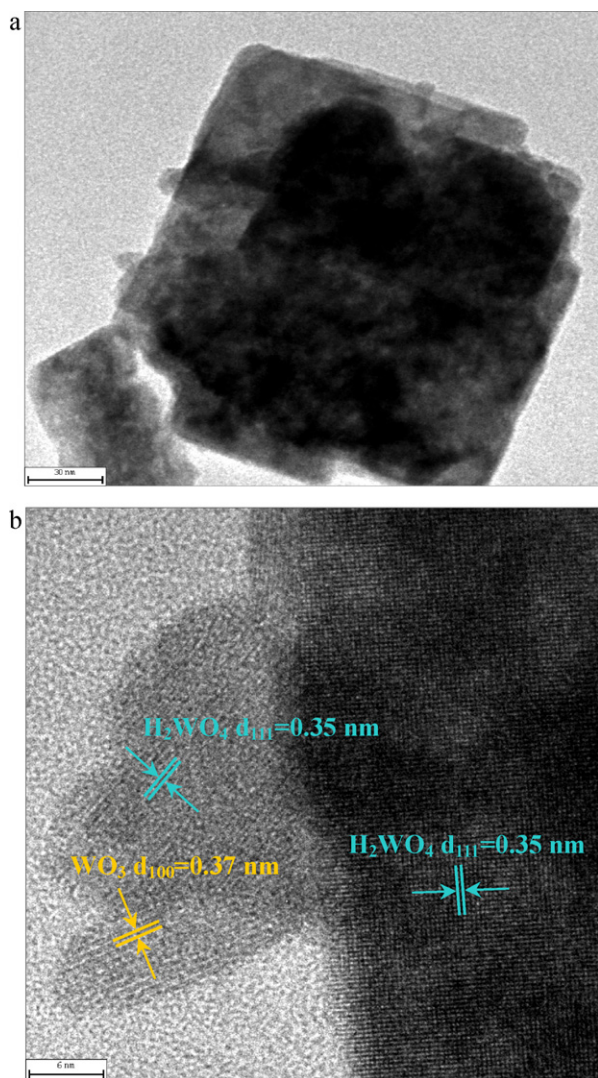

Fig. 7. (a) TEM and (b) HRTEM images of 57.10%WO_3/H_2WO_4.

485 nm in the visible light region, respectively. The WO_3/H_2WO_4 heterostructures exhibited a mixed absorption property of both WO_3 and H_2WO_4. With decreasing WO_3 contents, the absorption edge of WO_3/H_2WO_4 had a clear monotonic red shift meanwhile the absorption intensity of WO_3/H_2WO_4 was enhanced gradually.
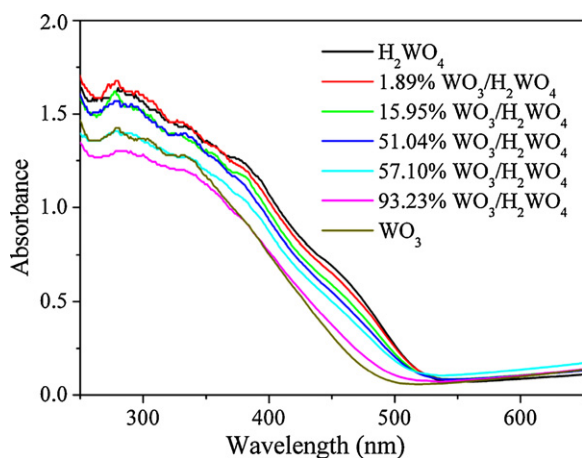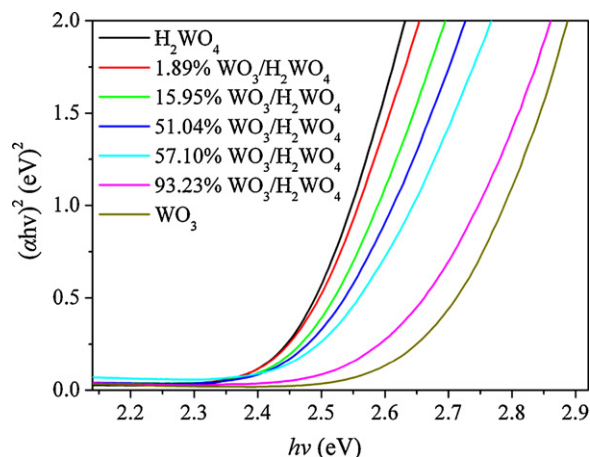

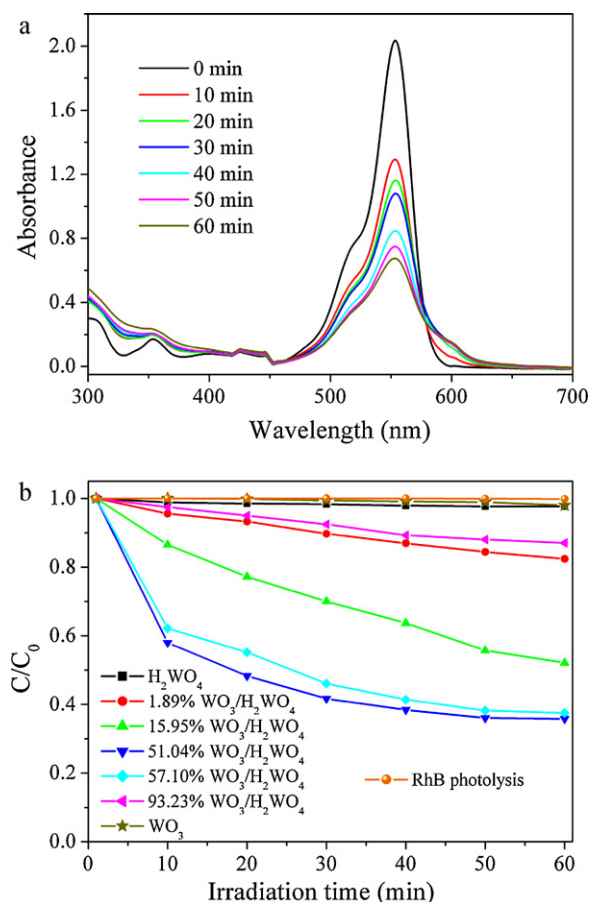**Fig. 8.** DRS of H_2WO_4, WO_3 and WO_3/H_2WO_4 heterostructures.

Fig. 10. (a) UV–vis spectral changes of RhB as a function of irradiation time over 51.04%WO_3/H_2WO_4 and (b) photocatalytic activities of H_2WO_4, WO_3 and WO_3/H_2WO_4 heterostructures on the degradation of RhB under visible light irradiation.

Fig. 11. k_{app} values of 51.04%WO_3/H_2WO_4 with different quenchers and under N_2-saturated condition.

seen, the photodegradation of RhB over single H_2WO_4 and WO_3 were merely 2.3% and 2.0%, respectively, after 60 min of visible light irradiation. Interestingly, the coupling of H_2WO_4 with WO_3 resulted in a sharp increase of RhB photodegradation.

For example, the 1.89%WO_3/H_2WO_4 could degrade 17.6% of RhB after 60 min of visible light irradiation. When the content of WO_3 increased, 47.9% and 64.2% of RhB could be degraded over 15.95% and 51.04%WO_3/H_2WO_4 after 60 min, respectively. However, when the content of WO_3 sequentially further increased, 57.10% and 93.23%WO_3/H_2WO_4 could degrade 62.5% and 13.0% of RhB after 60 min, less photocatalytically active than 51.04%WO_3/H_2WO_4. Therefore, 51.04%WO_3/H_2WO_4 exhibited the highest photocatalytic activity among as-prepared heterostructured WO_3/H_2WO_4. It should be clarified that when prolonging the irradiation time to 180 min, the degradation of RhB reached 85.1% over 51.04%WO_3/H_2WO_4, but no longer changed even continue extending irradiation time, which indicates that the photocatalytic activity of 51.04%WO_3/H_2WO_4 is still limited in our experiment and another way should be adopted to further enhance its activity. In addition, the reference experiments including dark adsorption of RhB by WO_3/H_2WO_4 heterostructures and photolysis of RhB without catalyst were also investigated. The results show that almost no RhB degradation occurred in the dark or by photolysis.

To further evaluate the effect of heterojunction on the photocatalytic activity of the WO_3/H_2WO_4 heterostructures, 51.04%WO_3/H_2WO_4 (0.100 g) were compared with the mechanically mixed counterpart sample 51.04%WO_3 + H_2WO_4 (0.051 g + 0.049 g) on the degradation of RhB under visible light
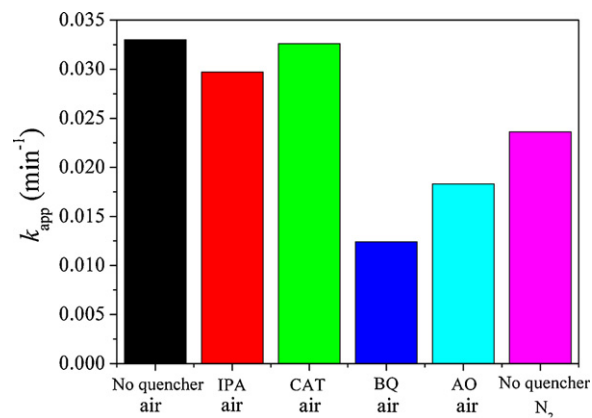
irradiation. 51.04%WO_3 + H_2WO_4 could degrade 11.3% of RhB after 60 min. Although 51.04%WO_3 + H_2WO_4 also exhibited better activity than that of pure WO_3 and H_2WO_4, its photocatalytic activity was much lower than that of the heterostructured sample 51.04%WO_3/H_2WO_4. This suggests the heterojunction formed between WO_3 and H_2WO_4 played a major role for the enhancement of photocatalytic activity.

According to the Langmuir–Hinshelwood (L–H) kinetics model [54–56], the photocatalytic process of RhB can be expressed as the following apparent pseudo-first-order kinetics equation [54]:

$$\ln\frac{C_0}{C} = k_{app}\, t \tag{8}$$

where k_{app} is the apparent pseudo-first-order rate constant (min^{-1}), C is RhB concentration in aqueous solution at time t (mg/L), C_0 is initial RhB concentration (mg/L). The k_{app} of as-prepared samples were respectively calculated and shown in Table 1. As can be seen, 51.04%WO_3/H_2WO_4 showed the highest value of k_{app} and corresponded to the best photocatalytic activity; whereas the k_{app} of the H_2WO_4 and WO_3 was almost negligible. Moreover, it can be seen that 51.04% and 57.10%WO_3/H_2WO_4 had much higher photocatalytic activities with k_{app} of 0.0330 and 0.0285 min^{-1}. The 1.89% and 93.23%WO_3/H_2WO_4 showed very low photocatalytic activities with k_{app} of 0.0036 and 0.0026 min^{-1}. This phenomenon can be attributed to the main factor, the function of heterojunctions. At the beginning of TD process, there are less WO_3/H_2WO_4 heterojunctions formed because the content of WO_3 is very low (0–1.89 wt%). This leads to limitations in separating the electrons and holes. With increasing WO_3 content the amount of heterojunctions increased, but at the higher WO_3 level (93.23–100 wt%) the heterojunctions will be destroyed due to the transformation from H_2WO_4 to WO_3. Therefore, with an appropriate ratio of H_2WO_4 and WO_3, the composites can exhibit perfect performance in photocatalysis.

3.3. Possible reaction mechanism

3.3.1. Roles of reactive species

The radicals and holes trapping experiments were designed to elucidate the PCO process. Fig. 11 displays the effects of different scavengers on the k_{app} of RhB degradation over 51.04%WO_3/H_2WO_4. The more k_{app} is reduced, the more important role the oxidizing species play in the reaction [47]. As shown in Fig. 11, under irradiation the k_{app} was almost not changed when a •OH scavenger, isopropanol (IPA) [57,58], was added. This indicates that •OH are not the reactive species involved in the PCO process. In addition, the PL technique was also employed to detect •OH formed on the surfaces of the WO_3/H_2WO_4, as shown in Fig. 12. The principle is that TA readily reacts with •OH to produce highly fluorescent
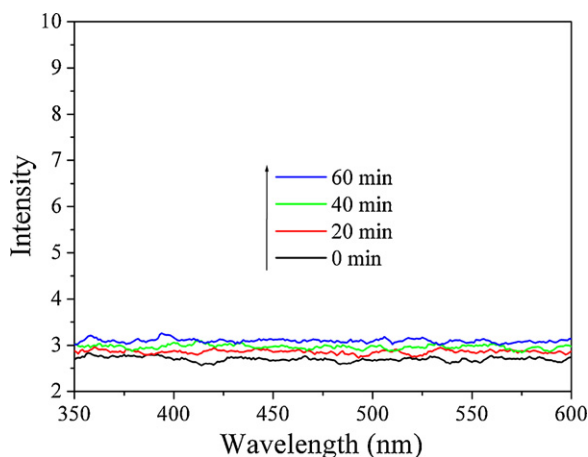
Fig. 12. •OH trapping PL spectra of 51.04%WO$_3$/H$_2$WO$_4$ in TA solution under visible light irradiation.

Fig. 13. Schematic diagram of electron–hole pairs separation and the possible reaction mechanism over heterostructured WO$_3$/H$_2$WO$_4$ photocatalyst under visible light irradiation.

product, 2-hydroxyterephthalic acid (HTA). The intensity of the PL peak of HTA is in proportion to the amount of •OH radicals produced in water [59,60]. This method relies on the PL signal at 425 nm of the hydroxylation of TA with •OH generated at the water/catalyst interface. It is clear that no PL signal was observed, demonstrating that no •OH were formed during the PCO process. These results show that •OH that are highly oxidative active species to many toxic organic pollutants, do not dominate the photodegradation procedure over WO$_3$/H$_2$WO$_4$ heterostructures.

On the other hand, the k_{app} could not decrease when a H$_2$O$_2$ scavenger, catalase (CAT) [47], was added, which shows that H$_2$O$_2$ is also not the reactive species involved in the PCO process. However, the k_{app} decreased obviously to 0.0124 and 0.0183 min^{-1}, respectively, in the presence of benzoquinone (BQ, •O$_2^-$ scavenger) [61,62] and ammonium oxalate (AO, h^+ scavenger) [48], which suggests that •O$_2^-$ and h^+ are the main reactive species for the degradation of RhB. The generation of •O$_2^-$ could be via photoinduced electrons reacting directly with O$_2$ adsorbed on the surface of the catalyst [1]. As shown in Fig. 11, the k_{app} decreased to 0.0236 min^{-1} under the anoxic suspension (N$_2$-saturated condition), indicating that O$_2$ is to primarily act as an efficient electron trap, leading to the generation of •O$_2^-$ and preventing the recombination of electrons and holes [63,64].

3.3.2. Possible degradation mechanism

In general, three possible reaction mechanisms should be considered for the RhB degradation, a photolysis process, a dye photosensitization process, and a photocatalytic process [65,66]. As a photolysis process, it can be described that the energy could be transferred from the induced dye to O$_2$ to produce a singlet oxygen atom (O(^{1}D)) that can work as an oxidant for the pure dye's photolysis [66,67], as shown from Eqs. (9)–(11).

$$RhB + h\nu(visible) \rightarrow RhB^* \tag{9}$$

$$RhB^* + O_2 \rightarrow RhB + 2O(^1D) \tag{10}$$

$$RhB + O(^1D) \rightarrow products \tag{11}$$

In Fig. 10b, the RhB degradation in the blank experiment under visible light irradiation could not be observed, which means that the RhB is stable [65,68] and the photolysis process has a negligible contribution to the degradation process of RhB. In other words, the RhB degradation maybe initiated possibly by a photocatalytic process or a photosensitization process.

For a dye photosensitization process, it means that the dye adsorbed on a catalyst is stimulated by light illumination to produce photoinduced electrons, and then the electrons can transfer
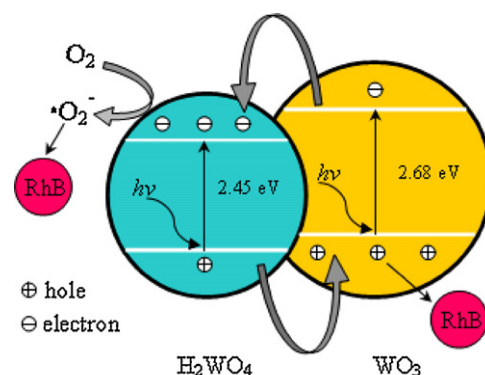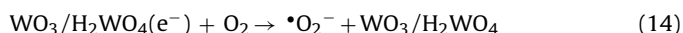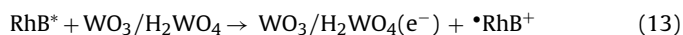
to the CB of the catalyst and react with O$_2$ to generate the •O$_2^-$ oxidant [66,69]. RhB is a xanthene dye that is widely known as a photosensitizer on TiO$_2$ and other oxides [65]. The maximum RhB absorption band is located at 554 nm, so the energy provided by the Xe lamp is enough for the photosensitization of the dye. The photosensitization process by RhB is well known for different systems [65,70,71]. In the case of WO$_3$/H$_2$WO$_4$ heterostructure, it can be described as follows:

$$RhB + h\nu(visible) \rightarrow RhB^* \tag{12}$$

$$RhB^* + WO_3/H_2WO_4 \rightarrow WO_3/H_2WO_4(e^-) + •RhB^+ \tag{13}$$

$$WO_3/H_2WO_4(e^-) + O_2 \rightarrow •O_2^- + WO_3/H_2WO_4 \tag{14}$$

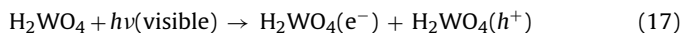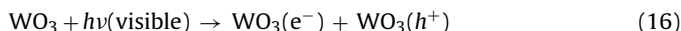$$•RhB^+ + •O_2^-(orO_2) \rightarrow products \tag{15}$$

As shown in Fig. 10b, the photodegradation of single H$_2$WO$_4$ and WO$_3$ was merely 2.9% and 2.0% via both the photocatalytic and the photosensitization mechanisms. This implies that the total effect of the photosensitization and the photocatalytic process, where the RhB degradation occurs over single H$_2$WO$_4$ or WO$_3$, is extraordinarily small. It is well known that a dye photosensitization mechanism is closely related to the basic characteristics of the dye, such as the structural stability of the dye, the adsorbability of the dye on catalyst surface, and the absorbance of the dye under solar irradiation [67]. As can be seen in Table 1, WO$_3$, WO$_3$/H$_2$WO$_4$ and H$_2$WO$_4$ have almost similar surface areas of 16.12–23.22 m^2/g, thus the adsorbabilities of RhB on as-prepared catalysts surfaces are almost the same. This implies that the RhB degradation over WO$_3$/H$_2$WO$_4$ on the basis of the photosensitization mechanism is neglectable. Therein, it is suggested that the decrease of RhB concentration in the WO$_3$/H$_2$WO$_4$ heterostructure system under visible light irradiation is initiated almost by a photocatalytic process.

In the photocatalytic process, it can be described that the promotion of an electron from the VB to the CB by light irradiation produces active site (hole) for the oxidation of the dye [65]. On the base of band gap structure of WO$_3$/H$_2$WO$_4$ and the effects of scavengers, possible pathway of the photocatalytic process with WO$_3$/H$_2$WO$_4$ was proposed. The specific schematic diagram of RhB degradation over WO$_3$/H$_2$WO$_4$ was illustrated in Fig. 13.

As can be seen in Fig. 13, for WO$_3$/H$_2$WO$_4$ system, both WO$_3$ and H$_2$WO$_4$ can be simultaneously excited to form electron–hole pairs under visible light irradiation. Subsequently photoinduced electrons transfer from the CB bottom of WO$_3$ to that of H$_2$WO$_4$. At the same time photoinduced holes also move in the opposite direction from the VB top of H$_2$WO$_4$ to that of WO$_3$. After that, electrons react with O$_2$ adsorbed on the surface of catalyst to generate reactive •O$_2^-$ that induced the degradation of RhB. Meanwhile, reactive

holes can directly degrade RhB. The photocatalytic process can be described as follows:

$$WO_3 + h\nu(visible) \rightarrow WO_3(e^-) + WO_3(h^+) \tag{16}$$

$$H_2WO_4 + h\nu(visible) \rightarrow H_2WO_4(e^-) + H_2WO_4(h^+) \tag{17}$$

$$H_2WO_4(e^-) + O_2 \rightarrow {}^\bullet O_2^- + catalyst \tag{18}$$

$$RhB + {}^\bullet O_2^- \rightarrow products \tag{19}$$

$$RhB + WO_3(h^+) \rightarrow products \tag{20}$$

In a word, the WO_3/H_2WO_4-assisted photodegradation of RhB occurs via two processes: a photocatalytic process and the photosensitized process. Both the photocatalytic process and the photosensitized process would work concurrently under visible light irradiation. However, the former is the predominant process due to the existence of heterojunction between H_2WO_4 and WO_3.

4. Conclusions

The WO_3/H_2WO_4 heterostructures with different contents of WO_3 were prepared by a simple thermodecomposition method through controlling reaction time at $300\,°C$. WO_3/H_2WO_4 exhibited enhanced photocatalytic activity compared to single WO_3 and H_2WO_4 over the degradation of RhB under visible light irradiation ($\lambda > 420\,nm$). The efficient separation of electrons and holes originated from the formation of WO_3/H_2WO_4 heterostructure benefited to obtain higher photocatalytic activity than WO_3 and H_2WO_4. ${}^\bullet O_2^-$ and h^+ played a major role for the degradation of RhB whereas ${}^\bullet OH$ and H_2O_2 can be negligible. This work provides a facile and efficient way to design composite heterostructured photocatalysts through thermodecomposition method.

References

[1] M.R. Hoffmann, S.T. Martin, W. Choi, D.W. Bahnemann, Chem. Rev. 95 (1995) 69–96.
[2] Z.G. Zhao, M. Miyauchi, Angew. Chem. Int. Ed. 47 (2008) 7051–7055.
[3] J. Kim, C.W. Lee, W. Choi, Environ. Sci. Technol. 44 (2010) 6849–6854.
[4] S.M. Sun, W.Z. Wang, S.Z. Zeng, M. Shang, L. Zhang, J. Hazard. Mater. 178 (2010) 427–433.
[5] H.W. Choi, E.J. Kim, S.H. Hahn, Chem. Eng. J. 161 (2010) 285–288.
[6] G.R. Bamwenda, H. Arakawa, Appl. Catal. A: Gen. 210 (2001) 181–191.
[7] K. Sayama, H. Hayashi, T. Arai, M. Yanagida, T. Gunji, H. Sugihara, Appl. Catal. B: Environ. 94 (2010) 150–157.
[8] W. Morales, M. Cason, O. Aina, N.R.D. Tacconi, K. Rajeshwar, J. Am. Chem. Soc. 130 (2008) 6318–6319.
[9] D. Chen, J.H. Ye, Adv. Funct. Mater. 18 (2008) 1922–1928.
[10] Z.G. Zhao, M. Miyauchi, J. Phys. Chem. C 113 (2009) 6539–6546.
[11] Y.F. Guo, X. Quan, N. Lu, H.M. Zhao, S. Chen, Environ. Sci. Technol. 41 (2007) 4422–4427.
[12] Q. Xiang, G.F. Meng, H.B. Zhao, Y. Zhang, H. Li, W.J. Ma, J.Q. Xu, J. Phys. Chem. C 114 (2010) 2049–2055.
[13] R. Abe, H. Takami, N. Murakami, B. Ohtani, J. Am. Chem. Soc. 130 (2008) 7780–7781.
[14] T. Arai, M. Horiguchi, M. Yanagida, T. Gunji, H. Sugihara, K. Sayama, Chem. Commun. (2008) 5565–5567.
[15] X.F. Cheng, W.H. Leng, D.P. Liu, J.Q. Zhang, C.N. Cao, Chemosphere 68 (2007) 1976–1984.
[16] J. Papp, S. Soled, K. Dwight, A. Wold, Chem. Mater. 6 (1994) 496–500.
[17] K.Z. Lv, J. Li, X.X. Qing, W.Z. Li, Q.Y. Chen, J. Hazard. Mater. 189 (2011) 329–335.
[18] D. Su, J.Y. Wang, Y.P. Tang, C. Liu, L.F. Liu, X.J. Han, Chem. Commun. 47 (2011) 4231–4233.
[19] T. Arai, M. Horiguchi, M. Yanagida, T. Gunji, H. Sugihara, K. Sayama, J. Phys. Chem. C 113 (2009) 6602–6609.
[20] C.C. Hu, J.N. Nian, H. Teng, Sol. Energy Mater. Sol. Cells 92 (2008) 1071–1076.
[21] D. Li, H. Haneda, J. Photochem. Photobiol. A: Chem. 160 (2003) 203–212.
[22] A.D. Paola, L. Palmisano, M. Derrigo, V. Augugliaro, J. Phys. Chem. B 101 (1997) 876–883.
[23] J. Cao, B.D. Luo, H.L. Lin, S.F. Chen, J. Hazard. Mater. 190 (2011) 700–706.
[24] P. Chatchai, Y. Murakami, S.Y. Kishiokal, A.Y. Nosaka, Y. Nosaka, Electrochim. Acta 54 (2009) 1147–1152.
[25] S.J. Hong, S. Lee, J.S. Jang, J.S. Lee, Energy Environ. Sci. 4 (2011) 1781–1787.
[26] S. Shamaila, A.K.L. Sajjad, F. Chen, J.L. Zhang, J. Colloid Interface Sci. 356 (2011) 465–472.
[27] Z.F. Liu, Z.G. Zhao, M. Miyauchi, J. Phys. Chem. C 113 (2009) 17132–17137.
[28] T. Arai, M. Yanagida, Y. Konishi, Y. Iwasaki, H. Sugihara, K. Sayama, J. Phys. Chem. C 111 (2007) 7574–7577.
[29] T. Huang, X.P. Lin, J.C. Xin, W.D. Wang, Z.C. Shan, F.Q. Huang, Mater. Sci. Eng. B 141 (2007) 49–54.
[30] X. Zhang, L.Z. Zhang, T.F. Xie, D.J. Wang, J. Phys. Chem. C 113 (2009) 7371–7378.
[31] H.F. Cheng, B.B. Huang, Y. Dai, X.Y. Qin, X.Y. Zhang, Langmuir 26 (2010) 6618–6624.
[32] Y. Yoshinaga, M. Kudo, S. Hasegawa, T. Okuhara, Appl. Surf. Sci. 121–122 (1997) 339–342.
[33] H.M. Yang, R.R. Shi, K. Zhang, Y.H. Hua, A.D. Tang, X.W. Li, J. Alloys Compd. 398 (2005) 200–202.
[34] T. Hyeon, Chem. Commun. (2003) 927–934.
[35] J. Park, K. An, Y. Hwang, J.G. Park, H.J. Noh, J.Y. Kim, J.H. Park, N.M. Hwang, T. Hyeon, Nat. Mater. 3 (2004) 891–895.
[36] V.L. Calero-DdelC, A.M. Gonzalez, C. Rinaldi, J. Manuf. Sci. Eng. 132 (2010) 30914–30920.
[37] S.F. Chen, X.L. Yu, H.Y. Zhang, W. Liu, J. Hazard. Mater. 180 (2010) 735–740.
[38] C. Guery, C. Choquet, F. Dujeancourt, J.M. Tarascon, J.C. Lassegues, J. Solid State Electrochem. 1 (1997) 199–207.
[39] O. Yamaguchi, D. Tomihisa, H. Kawabata, K. Shimizu, J. Am. Ceram. Soc. 70 (1987) C-94–C-96.
[40] J.T. Szymanski, A.C. Roberts, Can. Mineral. 22 (1984) 681–688.
[41] F.G. Wang, C.D. Valentin, G. Pacchioni, J. Phys. Chem. C 115 (2011) 8345–8353.
[42] J. Cao, B.D. Luo, H.L. Lin, S.F. Chen, J. Mol. Catal. A: Chem. 344 (2011) 138–144.
[43] F.H. Chung, J. Appl. Crystallogr. 8 (1975) 17–19.
[44] C.R. Hubbard, E.H. Evans, D.K. Smith, J. Appl. Crystallogr. 9 (1976) 169–174.
[45] A. Querejeta-Fernandez, M. Parras, A. Varela, F.D. Monte, M. Garcia-Hernandez, J.M. Gonzalez-Calbet, Chem. Mater. 22 (2010) 6529–6541.
[46] D.S. Wang, Y.D. Duan, Q.Z. Luo, X.Y. Li, L.L. Bao, Desalination 270 (2011) 174–180.
[47] G.T. Li, K.H. Wong, X.W. Zhang, C. Hu, J.C. Yu, R.C.Y. Chan, P.K. Wong, Chemosphere 76 (2009) 1185–1191.
[48] N. Zhang, S.Q. Liu, X.Z. Fu, Y.J. Xu, J. Phys. Chem. C 115 (2011) 9136–9145.
[49] M. Galceran, M.C. Pujol, C. Zaldo, F. Daz, M. Aguil, J. Phys. Chem. C 113 (2009) 15497–15506.
[50] H.I.S. Nogueira, A.M.V. Cavaleiro, J. Rocha, T. Trindade, J.D.P.D. Jesus, Mater. Res. Bull. 39 (2004) 683–693.
[51] M.F. Daniel, B. Desbat, J.C. Lassegues, B. Gerand, M. Figlarz, J. Solid State Chem. 67 (1987) 235–247.
[52] M.A. Butler, J. Appl. Phys. 48 (1977) 1914–1920.
[53] J. Zeng, H. Wang, Y.C. Zhang, M.K. Zhu, H. Yang, J. Phys. Chem. C 111 (2007) 11879–11887.
[54] Y. Li, X. Li, J. Li, J. Yin, Water Res. 40 (2006) 1119–1126.
[55] J.H. Sun, X.L. Wang, J.Y. Sun, R.X. Sun, S.P. Sun, L.P. Qiao, J. Mol. Catal. A: Chem. 260 (2006) 241–246.
[56] C.H. Wu, H.W. Chang, J.M. Chen, J. Hazard. Mater. 137 (2006) 336–343.
[57] L.S. Zhang, K.H. Wong, H.Y. Yip, C. Hu, J.C. Yu, C.Y. Chan, P.K. Wong, Environ. Sci. Technol. 44 (2010) 1392–1398.
[58] Y.X. Chen, S.Y. Yang, K. Wang, L.P. Lou, J. Photochem. Photobiol. A: Chem. 172 (2005) 47–54.
[59] K. Ishibashi, A. Fujishima, T. Watanabe, K. Hashimoto, Electrochem. Commun. 2 (2000) 207–210.
[60] Q. Xiao, Z.C. Si, J. Zhang, C. Xiao, X.K. Tan, J. Hazard. Mater. 150 (2008) 62–67.
[61] J. Bandara, J. Kiwi, New J. Chem. 23 (1999) 717–724.
[62] M.C. Yin, Z.S. Li, J.H. Kou, Z.G. Zou, Environ. Sci. Technol. 43 (2009) 8361–8366.
[63] Y.Y. Li, J.S. Wang, H.C. Yao, L.Y. Dang, Z.J. Li, J. Mol. Catal. A: Chem. 334 (2011) 116–122.
[64] Y.Q. Yang, G.K. Zhang, S.J. Yu, X. Shen, Chem. Eng. J. 162 (2010) 171–177.
[65] A.M.D. Cruz, U.M.G. Perez, Mater. Res. Bull. 45 (2010) 135–141.
[66] X.P. Lin, T. Huang, F.Q. Huang, W.D. Wang, J.L. Shi, J. Phys. Chem. B 10 (2006) 24629–24634.
[67] W.S. Kuo, P.H. Ho, Dyes Pigments 71 (2006) 212–217.
[68] T.B. Li, G. Chen, C. Zhou, Z.Y. Shen, R.C. Jin, J.X. Sun, Dalton Trans. 40 (2011) 6751–6758.
[69] C. Nasr, K. Vinodgopal, L. Fisher, S. Hotchandani, A.K. Chattopadhyay, P.V. Kamat, J. Phys. Chem. 100 (1996) 8436–8442.
[70] Y. Zhao, C.Z. Li, X.H. Liu, F. Gu, H.L. Du, L.Y. Shi, Appl. Catal. B: Environ. 79 (2008) 208–215.
[71] P. Wilhelm, D. Stephan, J. Photochem. Photobiol. A: Chem. 185 (2007) 19–25.